


## Modeling Equatorial *F*-Region Ionospheric Instability Using a Regional Ionospheric Irregularity Model and WAM-IPE

D. L. Hysell<sup>1</sup> , T. W. Fang<sup>2</sup>, and T. J. Fuller-Rowell<sup>2,3</sup>

<sup>1</sup>Earth and Atmospheric Sciences, Cornell University, Ithaca, NY, USA, <sup>2</sup>Space Weather Prediction Center, Boulder, CO, USA, <sup>3</sup>University of Colorado, Boulder, CO, USA

**Key Points:**

- Equatorial ionospheric *F*-region stability can be reproduced quantitatively using a regional data-driven direct numerical simulation (DNS)
- DNS model runs become forecasts when initialized and driven with parameters from a comprehensive GCM such as Whole Atmosphere Model with Ionosphere, Plasmasphere, Electrodynamics
- The post-sunset background vertical plasma drift and zonal thermospheric wind profile are the most critical forecast parameters

**Correspondence to:**

D. L. Hysell,  
david.hysell@cornell.edu

**Citation:**

Hysell, D. L., Fang, T. W., & Fuller-Rowell, T. J. (2022). Modeling equatorial *F*-region ionospheric instability using a regional ionospheric irregularity model and WAM-IPE. *Journal of Geophysical Research: Space Physics*, 127, e2022JA030513. <https://doi.org/10.1029/2022JA030513>

Received 31 MAR 2022

Accepted 14 AUG 2022

**Author Contributions:**

**Conceptualization:** D. L. Hysell

**Data curation:** D. L. Hysell

**Formal analysis:** D. L. Hysell, T. J. Fuller-Rowell

**Funding acquisition:** T. W. Fang

**Methodology:** D. L. Hysell, T. W. Fang

**Project Administration:** T. W. Fang

**Resources:** D. L. Hysell, T. W. Fang

**Software:** D. L. Hysell, T. W. Fang

**Validation:** D. L. Hysell, T. W. Fang, T. J. Fuller-Rowell

**Visualization:** D. L. Hysell

**Writing – original draft:** D. L. Hysell

**Writing – review & editing:** T. W. Fang, T. J. Fuller-Rowell

**Abstract** This paper uses a regional simulation of plasma convective instability in the postsunset equatorial ionosphere together with a global atmosphere/ionosphere/plasmasphere GCM (WAM-IPE) to forecast irregularities associated with equatorial spread *F* (ESF) for 1–2 hr after sunset. First, the regional simulation is initialized and forced using ionosphere state parameters derived from campaign data from the Jicamarca Radio Observatory and from empirical models. The irregularities produced by these simulations are found to be quantitatively similar to those observed. Next, the aforementioned state parameters are replaced with parameters from WAM-IPE, and the resulting departures between the simulated and observed irregularities are noted. In one of five cases, the forecast failed to accurately predict ESF irregularities due to the late reversal of the zonal thermospheric winds. In four of five cases, significant differences between the observed and predicted prereversal enhancement (PRE) of the background vertical drifts resulted in degraded forecast accuracy. This highlights the need for improved PRE forecasting in the global-scale model.

### 1. Introduction

This paper describes an ongoing effort to model and forecast plasma density irregularities in the postsunset equatorial *F*-region ionosphere, the phenomenon responsible for ionogram spreading (“equatorial spread *F*” or ESF) and a wide range of related space-weather effects (see reviews by Ossakow (1981), Woodman (2009), Kelley et al. (2011), and Kil (2015)). The irregularities are understood to be produced by interchange instabilities drawing free energy from the steep bottomside plasma density gradient and the associated flow that form at sunset. The theory of ionospheric interchange instability is well explored and relatively straightforward, although complexity grows when the effects of ion inertia, neutral winds, shear flow, finite parallel conductivity, and electromagnetism are considered (e.g., Dao et al., 2013; Guzdar et al., 1983; Keskinen et al., 2003; Zalesak et al., 1982; Zargham and Seyler, 1989). Despite the simplicity of the underlying instability, a forecast method outperforming climatological forecasts has yet to be demonstrated.

For most of the last 50 years, methods for assessing the likelihood of instability have centered on evaluating the linear instability growth rate using the field-line integration formalism introduced by Haerendel (1973) and simplified by Sultan (1996). Haerendel introduced the method to test whether field-line integration could explain the then mysterious observation of irregularities in the topside (it could not). The method is now applied broadly to the problem of identifying favorable conditions for instability, as put to practice recently by Wu (2015), Ajith et al. (2016), Shinagawa et al. (2018), and Tang et al. (2020). While the method is expedient, and while it may give a qualitative indication of the likelihood of observing irregularities in some circumstances, it lacks rigorous mathematical and physical foundations, as described below. Its efficacy needs to be tested systematically in any case. A clue that the analysis is misleading is the fact that the *e*-folding time is seldom calculated to be less than 1,000 s, and seldom for very long. Predicted growth rates are therefore too slow to account for the appearance of highly developed depletion plumes penetrating well into the topside within 90 min of sunset, something that is often observed (Chapagain et al., 2009; Hysell & Burcham, 2002; Smith et al., 2016) (see also below).

A partial lists of problems with the aforementioned method include: (a) Recombination should not appear in the calculation (Huba et al., 1996). (b) The formula given by Sultan (1996) neglects significant spatial variations in the driving terms (vertical plasma drift, vertical neutral wind, and gravity) which need to be included in the integration kernels with appropriate weighting (Ge et al., 2018; Hysell et al., 2006). (c) Magnetic field lines are not equipotentials, and the flux-tube integration formalism neglects important parallel-to-B thermal effects which alter dynamics and stability (e.g., Drake and Huba, 1987). (d) The linear, local instability growth rate result

assumes plane-wave eigenfunctions which only apply when the coefficients in the state equations are constants, which they are not. More complicated eigenfunctions must be sought when determining the fastest-growing modes (e.g., Satyanarayana et al., 1984; Zargham and Seyler, 1987). (e) When shear flow is present, the eigenfunctions may be neither normal nor complete, and eigenfunction analysis can no longer be relied upon to predict the fastest growing irregularities in any case (Flaherty et al., 1999; Trefethen et al., 1993). (f) Nonlinear effects can influence irregularity development before and as plumes form (e.g., Hysell and Seyler, 1998; Keskinen et al., 2003; Zalesak et al., 1982).

Perhaps most importantly, the conventional Haerendel (1973) formalism neglects the destabilizing effects of purely zonal neutral thermospheric winds that can excite obliquely propagating waves (with respect to the horizontal) which can grow much more rapidly than the zonally propagative waves excited by the background zonal electric field, vertical winds, or gravity (Hysell et al., 2006; Hysell & Kudeki, 2004). These waves seem to be essential to account for the appearance of topside irregularities within 90 min of instability onset during quiet-time conditions.

The goal of the present effort is to model irregularity occurrence accurately on a day-to-day basis for one 2 hr after sunset. We assert that the gold standard for irregularity forecasting presently is direct numerical simulation of potentially unstable ionospheric regions incorporating the most important instability drivers and with accurate initial conditions. Our effort so far has involved initializing and driving a regional ionospheric irregularity model using incoherent scatter radar (ISR) measurements from the Jicamarca Radio Observatory supported by some tuned empirical and physics-based models (see Hysell et al. (2015) and references therein). Modeling is normally initialized around sunset and then evaluated approximately 2 hr later, the results compared with coherent scatter radar observations of the irregularities that actually occurred.

The aforementioned outcome is not a forecast, however, owing to the requirement of concurrent information about the forcing (background zonal electric field and neutral wind profiles mainly) throughout the simulation. In this paper, we modify the procedure, extracting the information needed to initialize and force the regional simulation from a global atmospheric ionospheric model, Whole Atmosphere Model with Ionosphere, Plasmasphere, Electrodynamics (WAM-IPE). WAM-IPE is running operationally at the National Oceanic and Atmospheric Administration Space Weather Prediction Center (NOAA-SWPC) and used to forecast the background conditions that control the regional model.

Below, we describe an experimental campaign conducted at the Jicamarca Radio Observatory in September 2021, which provided data for our forecast analysis. After describing the regional irregularity model and WAM-IPE, we perform a series of tests designed to assess the combined model forecast strategy. Results from the tests are then summarized.

## 2. Campaign Results

Experiments were performed at the Jicamarca Radio Observatory between 21 and 25 September 2021, a geomagnetically quiet period. The experiments included ISR measurements of plasma number density, electron and ion temperature, zonal plasma drift, and vertical plasma drift profiles. Experiments also included observations of coherent scatter from 3 m plasma density irregularities including imaging measurements. The former provide information for initializing and forcing the regional irregularity model whereas the latter provide information for assessing the accuracy of the model results. Similar experimental campaigns combined with regional model assessments have been performed a number of times in recent years—see Hysell et al. (2015) and references therein for details. The results presented here are typical of all the results accumulated and published to date.

Figure 1 shows incoherent scatter data from Jicamarca for the postsunset hours of 24 and 25 September 2021. The panels in the figure show information about electron number density, zonal plasma drift speed, and vertical plasma drift speed versus altitude and time. Note the presence in the data of a modest prereversal enhancement in the background vertical drifts and strong vertical shears in the zonal plasma drifts after sunset.

ISR data such as these are used both to initialize and drive the regional irregularity model described below. At the completion of model runs, the results can be compared with incoherent and coherent scatter radar data with respect to signatures of ionospheric irregularities. Note that no *F*-region plumes were observed on 24 and 25 September 2021 although some narrow bottom-type scattering layers were present at about 250 km altitude.

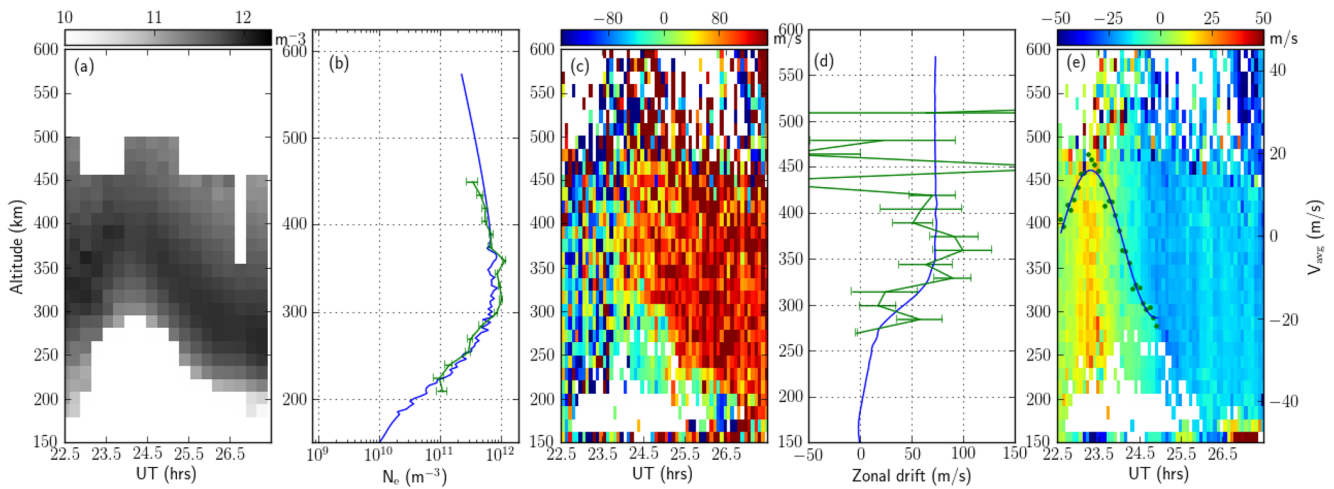


**Figure 1.** Example incoherent scatter radar data versus universal time and altitude for 24 and 25 September 2021. Note that  $UT = LT + 5$  hr. From left to right, the panels depict electron density (a), electron density profiles at 2300 UT (1800 LT) (b), zonal plasma drifts (c), zonal plasma drift profiles at 0000 UT (1900 LT) (d), and vertical plasma drifts (e). Superimposed on the rightmost panel are height-averaged vertical drifts versus time plotted against the scale at the extreme right. Green curves represent observations whereas blue curves are model values (see text). No  $F$ -region plumes were observed during the times shown.

Where irregularities are present, they interfere with the incoherent scatter technique, leaving blank patches in the various data fields represented here.

Model initialization will take place at 2300 UT. The electron density profile at 2300 UT is shown in Figure 1, second panel from the left, as a green curve. The corresponding profile in the irregularity model at initialization time over Jicamarca's location is shown as a blue curve. The model electron density specification at all locations is initialized using the SAMI2-PE model (SAMI2 is Another Model of the Ionosphere with Photoelectrons), where the equivalence of local time and longitude is assumed (see below). SAMI2-PE can be 'tuned' for optimal congruity with data through the adjustment of the F10.7 solar flux parameter and parameters controlling the time history of the background electric field. In this and every case during the campaign, no tuning was required for satisfactory model-data agreement at the time of initialization. Ion composition is initialized using the International Reference Ionosphere model (IRI-2016). We could also use SAMI2-PE for the initial ion composition specification, but this approach is more flexible, allowing the exchange of SAMI2-PE with other tools that do not include composition (e.g., the Parametrized Ionospheric Model (PIM), ionosonde-derived profiles, etc.)

The winds to be applied throughout the model run are derived from the Horizontal Wind Model (HWM14—see below). The winds in the simulation are based on HWM14 but tuned to make the measured and modeled zonal plasma drifts consistent. Here, the zonal drift profile measured at 0000 UT is shown in the second panel to the right in green whereas the model drifts at that time are shown in blue. Tuning in this context generally means the application of a multiplicative constant. In this and every case during the campaign, no tuning was required for satisfactory model-data agreement.

Note that the galactic center, the main source of noise in the radar measurements, passed directly over the Jicamarca radar during the experiments, significantly degrading the signal-to-noise ratio and the data quality between about 2200 and 0030 UT (1700–1930 LT). The effect is most evident in the zonal drift measurements which have the highest experimental uncertainties, being derived from the difference of line-of-sight drift measurements from two closely spaced near-vertical beams. The model winds and zonal plasma drifts were therefore assessed against the measurements an hour after model initialization in this case when uncertainties in the data were smaller.

The ISR campaign data do not indicate very significant differences in the initial conditions circa 2300 UT or the background thermospheric winds on different campaign nights, and so we focus on day-to-day variations in the background vertical drifts. Figure 2 shows the vertical drift data for the entire campaign. The behavior of the background vertical drifts and the prereversal enhancement in particular varied dramatically from night to night, as is typical even during quiet times (Fejer, 1997). The occurrence of  $F$ -region irregularities and radar

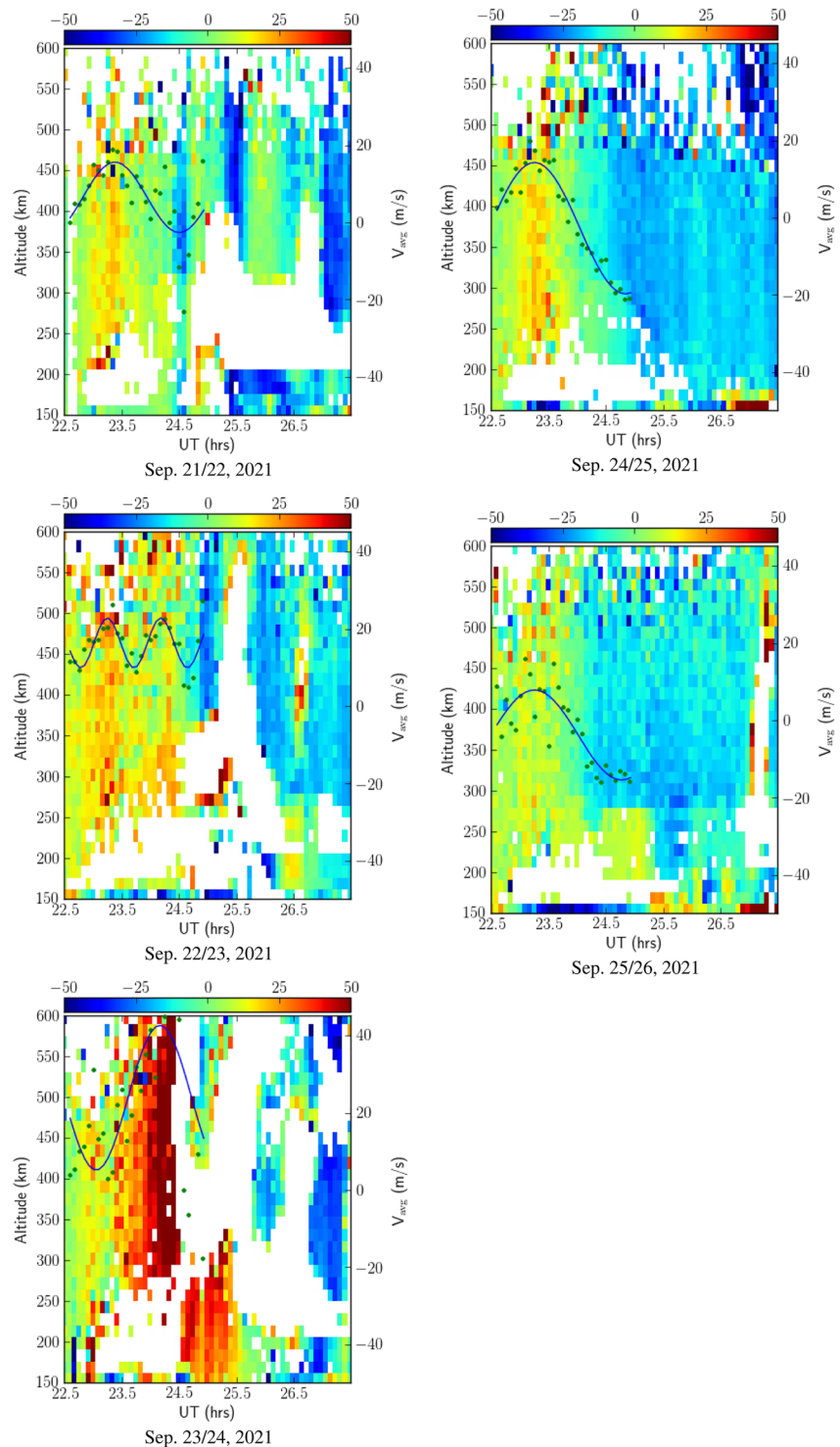


**Figure 2.** Vertical plasma drift data from Jicamarca similar to the rightmost panel in Figure 1 except for all five campaign days. Height-averaged vertical plasma drifts are plotted against the scale on the right of each panel. Blank patches in the  $F$ -region in the data field are indicative of coherent scatter, irregularities, and equatorial spread  $F$  plumes.

plumes also varied drastically from night to night, as indicated indirectly in Figure 2 by blank patches where the incoherent scatter technique could not be applied. Backscatter plumes reached an altitude of 400 km by 0100 UT on 21 and 22 September, 600 km by 0100 UT on 22 and 23 September, and 600 km by 0030 UT on 23 and 24

September when they exited the upper boundary of the plotted data set. Only bottom-type irregularities, which are nearly ubiquitous over Jicamarca, were present on 24 and 25 September 2021 and 25 and 26 September 2021.

While irregularity development appears to be correlated at least superficially with the intensity and duration of the prereversal enhancement, a quantitative association requires direct numerical simulation. Such simulations were undertaken as described below. The ultimate goal of this work is to be able to perform such simulations before the radar data are acquired.

### 3. Model Descriptions

The regional ionospheric irregularity model used here was described in detail by Hysell et al. (2018). The model has two components. One component is a linear potential solver that solves the quasineutrality condition for the perturbed electrostatic potential in three dimensions. The solver considers Pedersen, Hall, and direct currents along with thermal currents associated with perpendicular, diamagnetic, and parallel diffusion and currents due to gravity. The solver uses a conjugate gradient method with ILU (incomplete lower upper) preconditioning and pivoting. Mixed (Robin) boundary conditions are used in each spatial dimension. The spatial resolution is of the order of a few km in each dimension.

The model is cast in magnetic dipole coordinates and considers  $\text{NO}^+$ ,  $\text{O}_2^+$ ,  $\text{O}^+$ , and  $\text{H}^+$  ions together with electrons. The second component of the model is a finite-volume code which advances the ion species forward in time according to the equation of motion for ion dynamics which are solved explicitly. The model uses a flux assignment scheme based on the total variation diminishing (TVD) condition. It incorporates monotone upwind schemes for conservation laws (MUSCLs) with flux limiting and a second-order TVD scheme to minimize diffusion and dispersion. Dimensional splitting is used to extend the technique to three dimensions. A second-order Runge Kutta scheme is used for time advance with a nominal step size of 7.5 s. For a detailed description of the methodology, see Trac and Pen (2003) and references therein.

A number of supporting empirical and physics-based models are normally incorporated into regional model runs. These include NRLMSIS 2.0 for neutral atmospheric parameter specification, IRI-2016 for initial ion composition, SAMI2-PE for initial background electron densities, and HWM14 for neutral winds (Bilitza et al., 2016; Drob et al., 2015; Emmert et al., 2021; Varney et al., 2012) (SAMI2-PE is a two-dimensional model which is run at a single longitude; to extrapolate the results to adjacent longitudes, the equivalence of local time and longitude is assumed.) In numerous previous experiments, it was found that SAMI2-PE and HWM14 can generally be tuned to produce good agreement with Jicamarca measurements on a day-to-day basis (see also Varney et al. (2013)). Tuning in the case of SAMI2-PE amounts to modifying the 10.7 cm solar flux parameter to optimize congruity with ISR-derived electron density profiles. In the case of HWM14, tuning means multiplicative scaling of the winds to optimize congruity with ISR-derived zonal plasma drift profiles. In addition, regional model runs are normally forced with background vertical plasma drift measured directly with incoherent scatter.

All instability models require variances or seed noise in the initial conditions which then either grow or do not grow depending on the availability of free energy and a growth mechanism. This is not normally considered physically significant as variance is present in all of nature. For the regional ionospheric model used here, the initial number density specification includes additive Gaussian white noise. We are agnostic about the source of the variance in nature, which could result from a number of processes, but note that no adjustment or 'tuning' of the noise is required to achieve day-to-day agreement with radar observations.

WAM-IPE has been in operation at NOAA-SWPC since July 2021. The Whole Atmosphere Model is an extension of the National Weather Service (NWS) operational Global Forecast System (GFS) General Spectral Model (GSM) (e.g., Akmaev and Juang (2008)), which is used for the nation's global and regional weather forecasts. To create WAM, the weather model was extended from 64 to 150 layers, with the top altitude level raised from 62 to about 600 km in the upper atmosphere. The current WAM configuration is based on an extension of the GFS spectral dynamical core into the mesosphere and thermosphere with the lower and upper atmosphere physics incorporated via the vertical column interface. Included processes are: radiative transfer, hydrological cycle, planetary boundary layer and surface exchange, orographic gravity waves, and vertical eddy mixing. The vertical extension of the model domain required additional physical processes, including UV and EUV radiative heating, infrared radiative cooling with the breakdown of local thermodynamic equilibrium, non-orographic gravity

waves, ion drag, Joule heating, and horizontal and vertical molecular dissipative processes. A Whole atmosphere Data Assimilation System (WDAS) that utilizes the 3-dimensional variational (3DVar) analysis system GSI (Grid point Statistical Interpolation) is INCORPORATED in WAM. The current resolution of WAM with the hydrostatic dynamical core runs at T62 spectral truncation, which is equivalent to a Gaussian grid spacing of  $\sim 180$  km and can resolve waves longer than about 500 km horizontal wavelengths with periods longer than about 15 min.

The IPE is a time-dependent, global, three-dimensional model of the ionosphere and plasmasphere. It provides plasma densities for nine ion species, thermal electron and ion temperatures, and both parallel and perpendicular velocities of the ionosphere and plasmasphere. A feature unique to the IPE model is the implementation of a more accurate representation of the Earth's magnetic field in conjunction with the well-tested Field Line Inter-hemispheric Plasma (FLIP) model (e.g., Richards et al., 2010) for parallel plasma transport along field lines. The realistic representation (IGRF-based) of the Earth's magnetic field combined with a self-consistent photoelectron calculation enables more accurate studies of the longitudinal and UT dependencies and hemispheric asymmetries.

The interhemispheric field lines in IPE covers the globe, from the magnetic equator to the pole, allowing the seamless transport of plasma perpendicular to magnetic field lines. The electric fields calculated by the electrodynamic solver (Richmond, 1995) are fed back to the plasma transport algorithm within the model. The Weimer model (Weimer, 2005) driven by the solar wind parameters is set by default to follow the highly variable magnetospheric convection at high latitudes. The current longitudinal resolution of IPE is  $4.5^\circ$ . The latitudinal resolution is variable and optimized to resolve the dynamical equatorial ionization anomaly (EIA) feature with latitudinal resolution of  $0.34^\circ$  (37 km at the foot-point of the flux tubes) equatorward of  $\pm 30^\circ$  magnetic latitude and  $\sim 1.3^\circ$  ( $\sim 143$  km at foot-points) poleward of  $\pm 30^\circ$  magnetic latitude. In total, there are 170 flux tubes at each longitude grid. The information exchange between WAM and IPE is carried out by remapping neutral atmospheric fields to IPE's magnetic grid at each coupling step. No ionosphere information is fed back to WAM currently.

The operational outputs including neutral parameters (winds, temperature, and compositions), plasma parameters (temperature, O+, H+, He+, N+, O2+, NO+, N2+ concentration), and ion drifts are used in this study. The model is driven by the observed solar flux F10.7 and solar wind parameters. The WDAS updated the lower atmosphere condition at 0 and 12 UT. While the output frequency is 3 min, the timestep for WAM and IPE are in 1 and 3 min, respectively.

## 4. Model Evaluation

Figure 3 shows the results of the regional direct numerical simulation for the five campaign nights in question. The simulations were initialized and forced according to the prescriptions above. Because of the similarity in the incoherent scatter measurements, the five simulations were initialized identically and forced with the same neutral winds. Only the background electric field specification differed. This day-to-day uniformity is unusual but affords an opportunity for some rather unambiguous modeling comparisons (see below).

Overall, the simulations have been able to anticipate the occurrence, occurrence time, and altitudes of interchange instabilities throughout the five campaign nights accurately. Note that the simulation is started and stopped at a given UT; Local times mentioned throughout the figures and captions shown refer to the local time at Jicamarca's location. The depletion plumes shown here reached an altitude of 400 km by 0100 UT on 21 and 22 September, 600 km by 0100 UT on 22 and 23 September, and 600 km by 0030 UT on 23 and 24 September. No depletion plumes formed on 24 and 25 September and 25 and 26 September, although weak irregularities formed at the base of the bottomside layer in both cases (so-called bottom-type layers). This behavior mimics closely the irregularities actually observed.

In the remainder of this paper, we will substitute various components of the regional model, incorporating parameters derived from WAM-IPE. We will do this progressively to assess the effects of replacing tuned and prescribed parameter with parameters that could actually be forecast. The results represent an important starting point for formulating a workable forecast strategy.

### 4.1. Background Parameters

The goal of this project is to eliminate the dependence of the regional irregularity simulation on empirical models and empirical data. The first step is to remove both NRLMSIS 2.0 and IRI-2016/SAMI2-PE and replace them

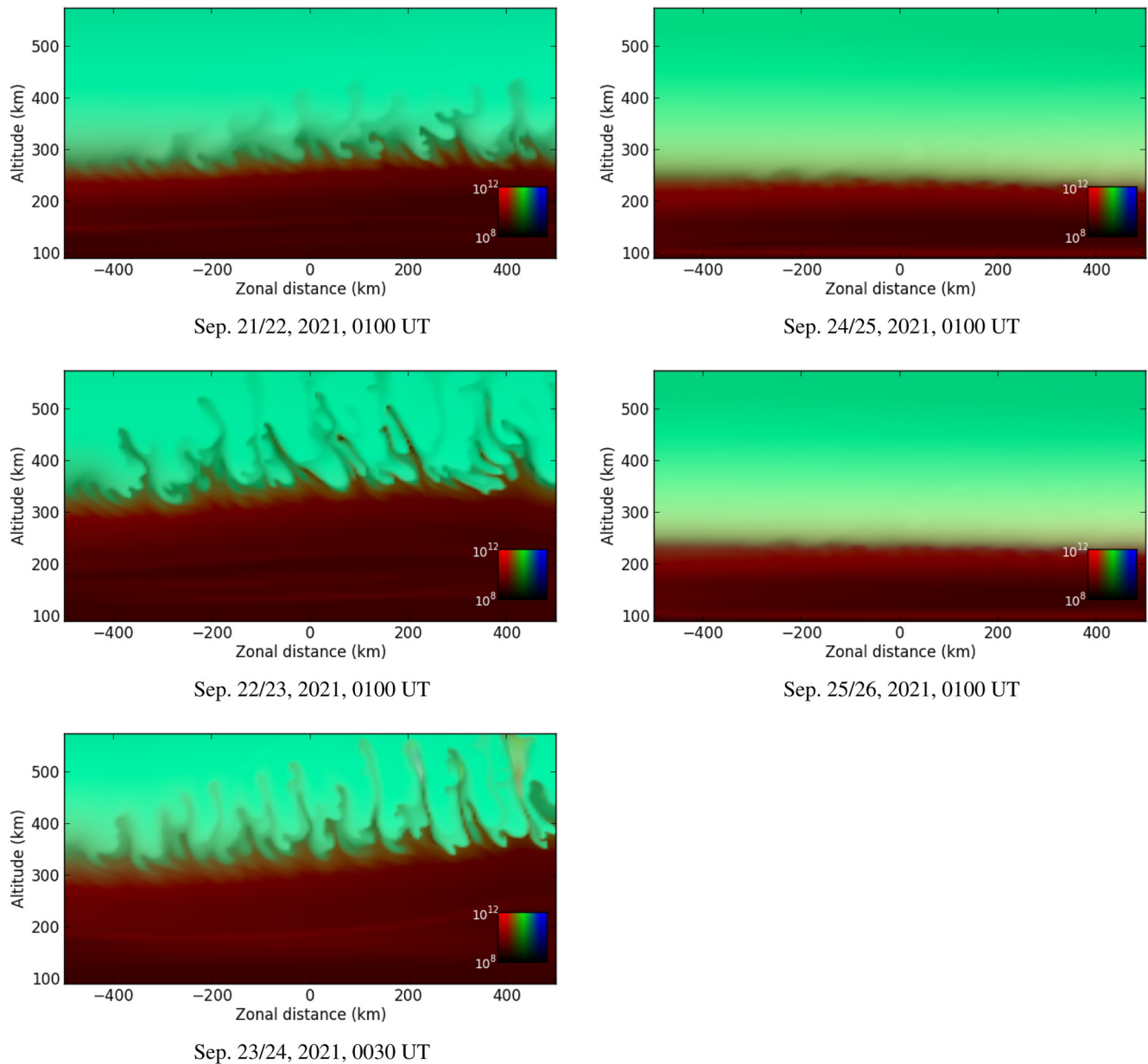


**Figure 3.** Regional simulations of the conditions over Jicamarca during the September campaign. Simulations were initialized at 2300 UT (1800 LT Jicamarca time) and concluded at the UT times shown. Cuts through the equatorial plane are shown versus altitude and east-west distance. The pixels represent both number density and composition according to the legend shown. Here, green, red, and blue hues represent atomic oxygen ions, molecular ions, and protons, respectively.

with WAM-IPE. WAM-IPE can supply a complete specification of the atmospheric composition and temperature throughout the simulations. It can also supply the initial conditions for the regional simulation with regard to plasma number density and composition.

Figure 4 shows the simulation outcomes for 21–25 September, 2021, from the regional irregularity simulation run under the conditions just described. These outcomes may be compared directly with those in Figure 3 to assess the effects on the forecast accuracy. Overall, the simulation outcomes remain qualitatively similar. The main difference is that the runs in Figure 4 exhibit a greater concentration of molecular ions in the bottomside than their counterparts in Figure 3. Close comparison also shows that the light-ion concentrations in Figure 4 in the topside are lower than in Figure 3. The depletion plumes in the 21 and 22 September run are arguably slightly

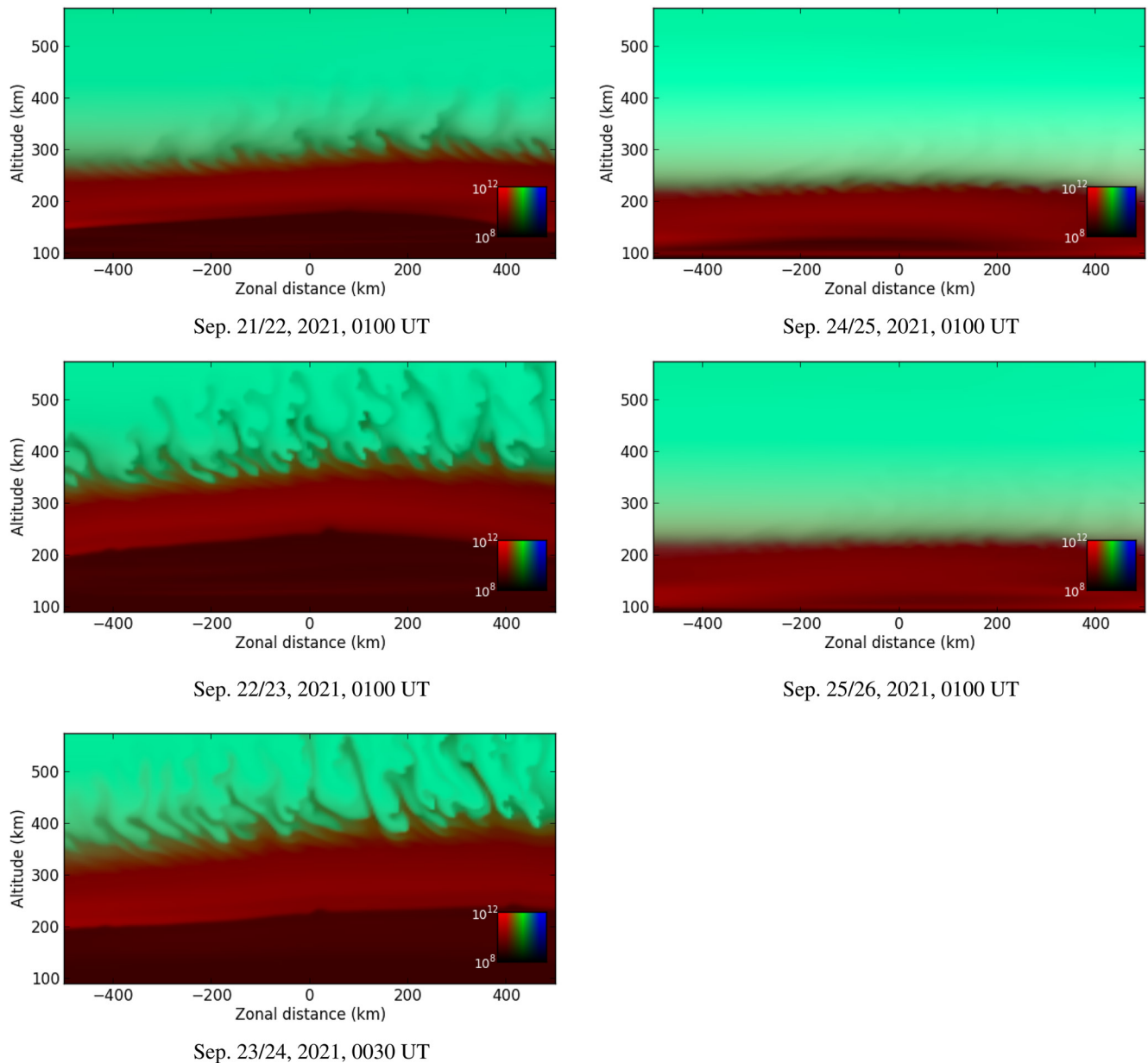


**Figure 4.** Same as Figure 3 only using background static atmospheric and ionospheric parameters from Whole Atmosphere Model with Ionosphere, Plasmasphere, Electrostatics (see text).

less developed in Figure 3 than they are in Figure 3, although the difference is not very significant. Overall, the accuracy of the recoveries of the radar measurements are comparable.

The differences in the runs are mainly indicative of differences in ionospheric composition produced by IRI-2016/SAMI2-PE and WAM-IPE. These differences are highlighted in Figure 5 which shows number density profiles for the various ion constituents at 2300 UT on 22 and 23 September 2021 at Jicamarca's location. Note that IRI-2016 normally introduces artificial discontinuities at 350 km altitude. Above (below) this altitude, molecular ions (light ions) are set identically to zero. Here, the discontinuities are removed by extending molecular and light-ion species through 350 km altitude with the assumption of a uniform scale height. The impact is not significant since the species involved are minor constituents in either case. We merely prefer not to have discontinuous inputs to the simulations.



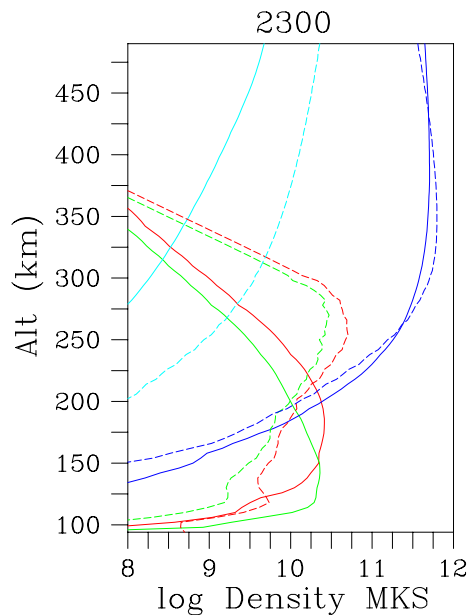


**Figure 5.** Ionospheric composition profiles used for stability modeling. The cyan, blue, red, and green curves represent  $H^+$ ,  $O^+$ ,  $NO^+$ , and  $O_2^+$  concentrations, respectively. Solid and dashed lines represent Whole Atmosphere Model with Ionosphere, Plasmasphere, Electrodynamics and SAMI2-PE/IRI-2016, respectively.

The atomic oxygen profiles from IRI-2016/SAMI2-PE and WAM-IPE are very similar except in the topside where IRI-2016/SAMI2-PE indicates a higher light-ion concentration—something that is consistent with observation (e.g., Derghazarian et al., 2021). The main difference between WAM-IPE and SAMI2-PE is that the latter indicates much more dense molecular ions in the bottomside and valley region. This leads to a much denser valley region overall, denser than is usually observed at Jicamarca at 1800 LT. The effect is to increase the conductive loading in the valley region somewhat which could cause modest decreases in the instability growth rate under some circumstances.

#### 4.2. Thermospheric Winds

More dramatic differences arise when, in addition to static parameters, dynamic parameters are exported from WAM-IPE to the regional irregularity model. Figure 6 shows the results of replacing the HWM14 winds in the irregularity simulations with WAM-IPE winds. While the simulation results are similar in four cases, in the case of Sep. 21/22, the effect of the WAM-IPE winds is to suppress instability, or nearly so. Understanding this outcome is critical.

Figure 7 compares the zonal neutral winds from HWM14 and WAM-IPE for 21 and 22 September 2021, at various local times. Overall, the wind profiles have comparable shapes and magnitudes in the upper thermosphere. The curves nearly converge the end of the simulation run. The crucial difference is the phasing of the winds and the relatively late turning of the WAM-IPE zonal winds from westward to eastward near the start of the run. Robust east-

ward winds are required to drive the vertical currents in the  $F$ -region responsible for the rapid onset and growth of irregularities at the base of the bottomside (Hysell & Kudeki, 2004). These irregularities are the cause of so-called bottom-type layers and serve to precondition the ionosphere for conventional collisional interchange instability. In this case, robust eastward winds emerged in WAM-IPE in the  $F$ -region only shortly before the reversal of the background zonal electric field. There was therefore insufficient time for preconditioning and subsequent irregularity growth to take place. The postsunset reversal of the WAM-IPE zonal winds occurred earlier in the 22 and 23 September and 23 and 24 September runs, and so vigorous instability was reproduced.

It is noteworthy here that zonal winds do not appear in the Haerendel (1973) growth-rate formula which is therefore incapable of distinguishing between ESF and non-ESF conditions, as demonstrated by the preceding set of model runs. Specifying the thermospheric winds and modeling the associated dynamo fields, vertical currents, and precursor instabilities are essential components of ESF forecasting.

#### 4.3. Background Vertical Plasma Drifts

Finally, we consider the specification of the background zonal electric field in the postsunset ionosphere. Figure 8 considers what happens when HWM14 winds are again incorporated in regional simulations but when the ISR-derived vertical plasma drifts are replaced with WAM-IPE prescriptions. In this case, congruity between the observed and simulated depletions is lost. The simulations in Figure 8 predict weak instability on 23 and 24 September versus fairly robust instability on 25 and 26 September, the opposite of what was actually observed. None of the five simulations reproduced the behavior of the ionosphere qualitatively, an outcome apparently no better than chance.

More insight into the simulations is provided by Figure 9 which compares the measured (by Jicamarca) and predicted (by WAM-IPE) background vertical drifts for the campaign interval in question. The figure highlights the correspondence between the prereversal enhancement of the zonal electric field and the robustness of the irregularities and the depletions that follow. Large prereversal enhancements, delayed reversals, and small post-reversal downdrafts appear to be conducive to instability. Irregularity forecasts can be expected to be no better than vertical drifts forecasts, as Figure 8 demonstrates.

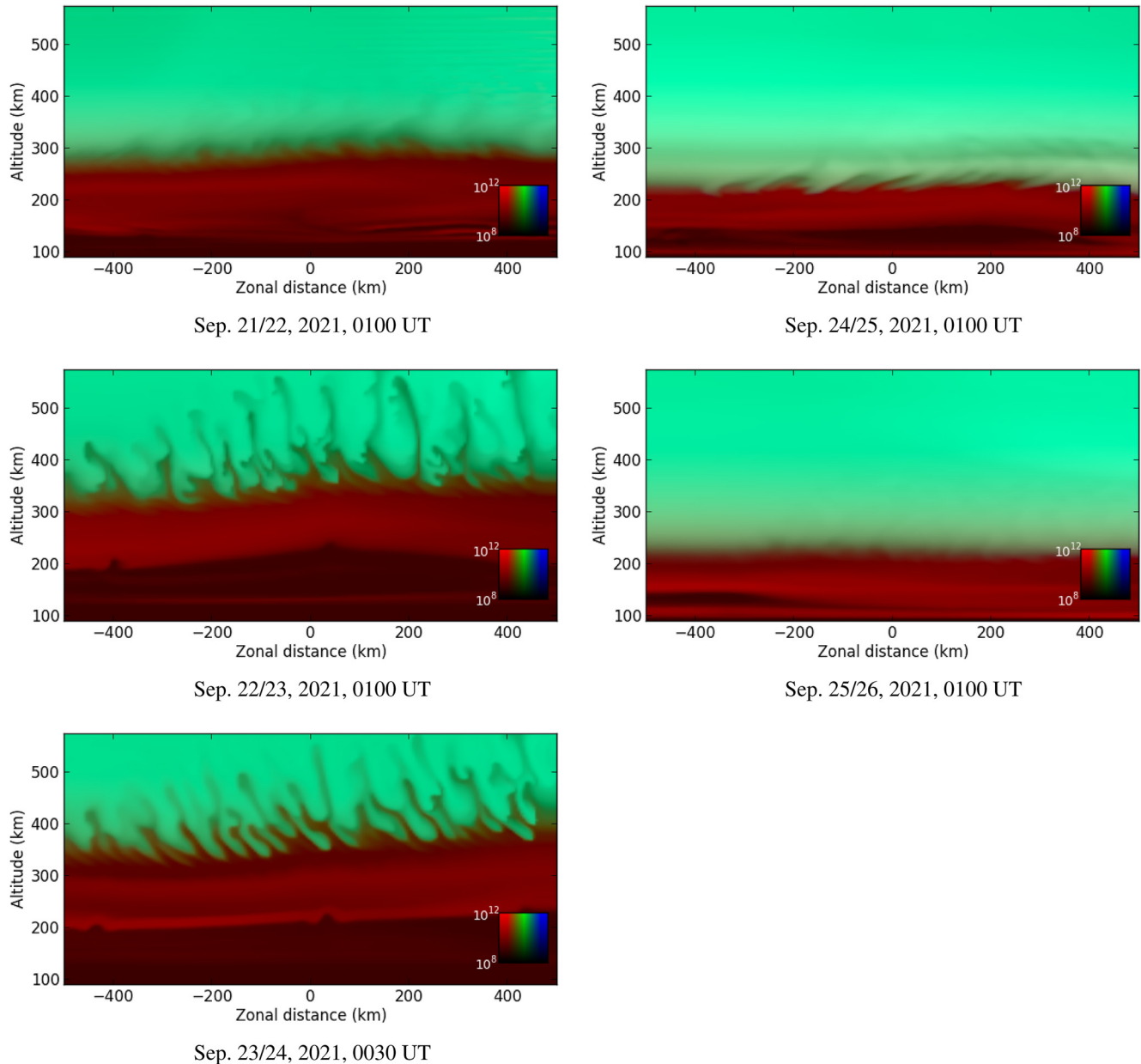


**Figure 6.** Same as Figure 4 only also using winds from Whole Atmosphere Model with Ionosphere, Plasmasphere, Electrodynamics (see text).

It is noteworthy that the vertical drifts measured on 21 and 24 September share similar time histories, at least through the first hour of the runs. As everything else about the model ionospheres was the same for the 2 days, linear growth rate calculations computed during the first hour of the runs would have produced similar results. The simulated outcomes were, in fact, strikingly different, as were the observed outcomes.

This highlights the importance of the timing of convective instability events which have three stages. In the first, rapidly growing irregularities driven by vertical currents precondition the bottomside, creating bottom-type layers. In the second, collisional interchange instability driven mainly by zonal electric fields deforms the entire bottomside incompressibly. Here, the intensity and duration of the prereversal enhancement are critical. In the third, currents driven by gravity sustain the growth of depletions as they penetrate into the topside. Not just the size of the prereversal enhancement but also the timing, particularly with respect to the reversal of the winds and the progress of irregularities developing toward the topside, appears to be crucial to the outcome.

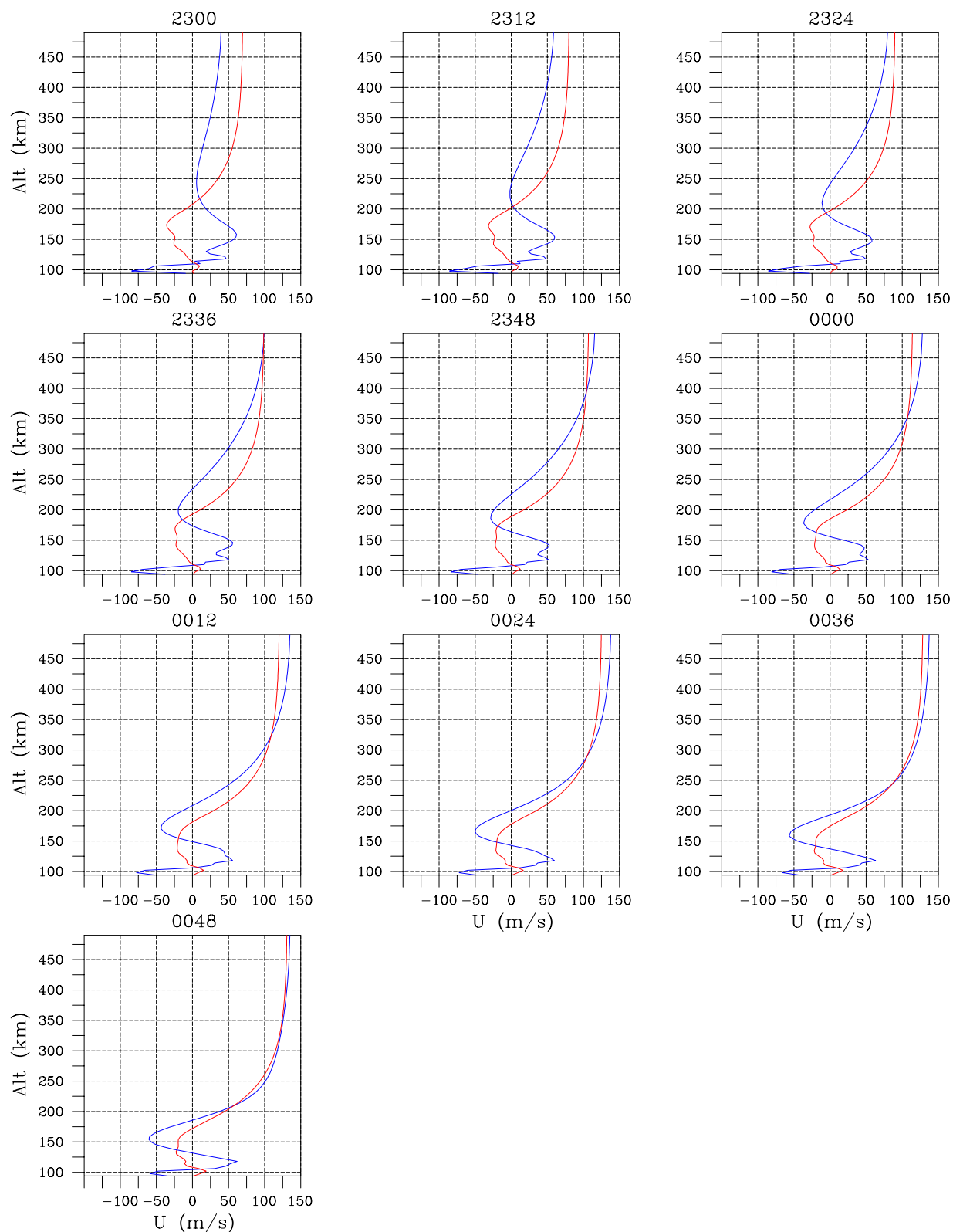


**Figure 7.** Zonal wind profiles used for stability modeling at different universal times on 21 and 22 September 2021. Blue (red) profiles represent Whole Atmosphere Model with Ionosphere, Plasmasphere, Electrodynamics (HWM14).

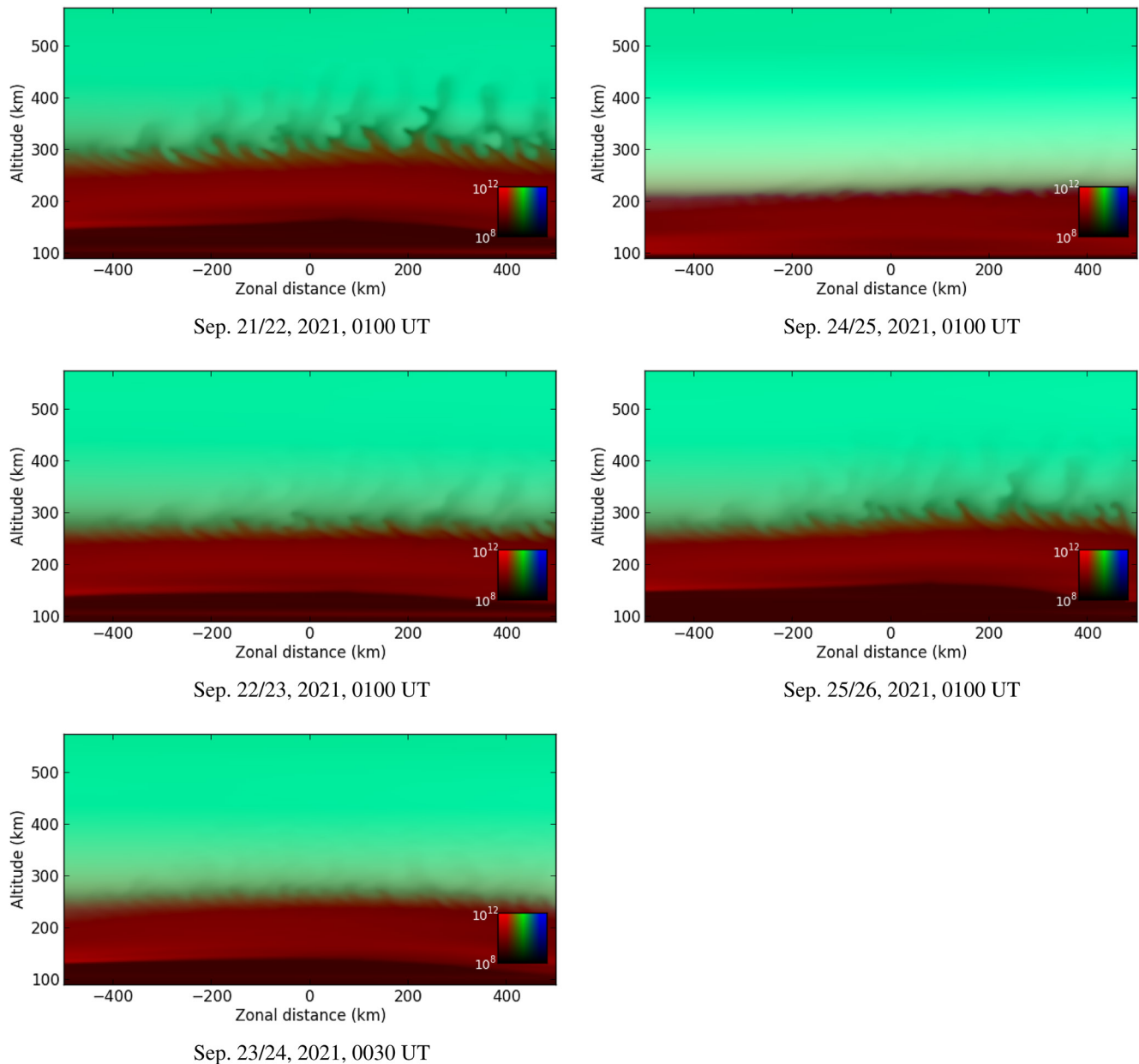


**Figure 8.** Same as Figure 4 only also using background zonal electric fields from Whole Atmosphere Model with Ionosphere, Plasmasphere, Electroynamics (see text).

## 5. Discussion and Conclusions

This paper reports on numerical simulations of convective instability in the equatorial ionosphere intended to reproduce observations of ionospheric irregularities during a September 2021 experiment campaign at Jicamarca. The timeframe of interest is the 1–2 hr period after sunset. The regional simulations were first initialized and forced on the basis of incoherent scatter state parameter measurements, and the simulation results were comparable to the irregularities that were actually observed in most important respects. The initial conditions, thermospheric wind forcing, and background electric field forcing were subsequently specified according to parameters extracted from WAM-IPE runs (While WAM-IPE runs can provide 2-day forecasts based on Kp forecasts, we did not attempt it in the current study.) The accuracy of the reproductions of the irregularities produced under these circumstances was significantly degraded, mainly due to disparities between measured and predicted background zonal electric fields and zonal thermospheric winds. While considerable progress has been made

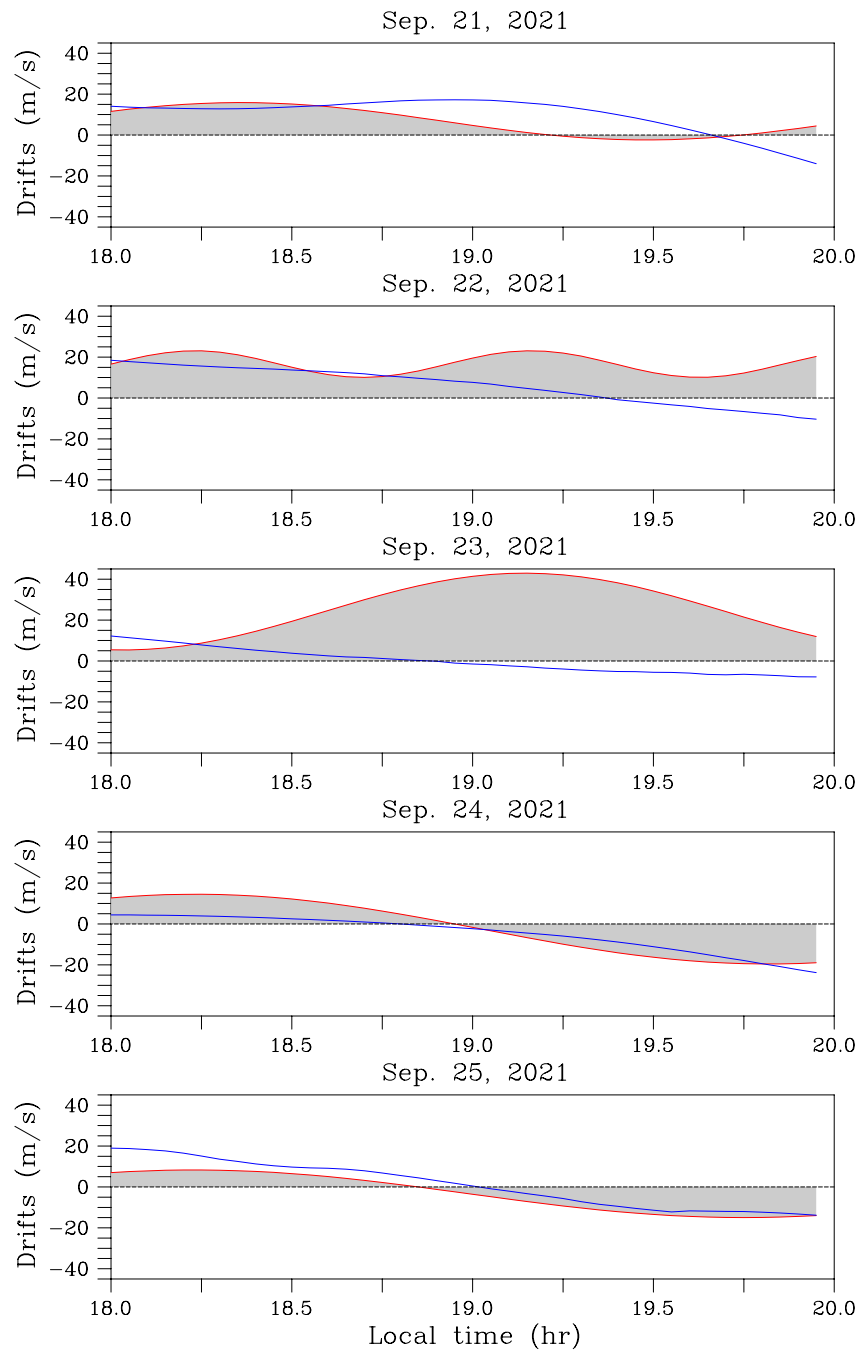


**Figure 9.** Vertical *F*-region plasma drifts used for stability modeling versus date and local time. Blue (red) curves represent Whole Atmosphere Model with Ionosphere, Plasmasphere, Electrodynamics (measured) drifts.

in understanding day-to-day ionospheric variability (see below), challenges clearly remain (Fang et al., 2018). Identifying the importance of overcoming these is the purpose of this paper.

WAM-IPE electrodynamics and phases of the zonal winds in the bottom side *F*-region are controlled by the filtering of the tides as they propagate from their sources in the lower atmosphere and stratosphere. The phases of tidal winds can be advanced or retarded by the direction of the background flow in the mesosphere and lower thermosphere. Data assimilation (DA) in WAM is currently only below 60 km altitude, which can constrain the dynamics in the source regions but the winds in the mesosphere and lower thermosphere are unconstrained. The results indicate the need to improve the WAM-IPE prediction of eastward electric fields and zonal winds. One

possibility to improve the prediction is to extend the WAM DA to higher altitudes (100 km) to assist with the tidal wind filtering. Although direct wind observations are sparse, satellite temperature measurements are available that can be used to constrain the winds, assuming the gradient wind balance condition. Ideally, the assimilation cycle should also be reduced from 6 to  $\sim 1$  hr to follow the observed tidal wind variations through the day. Other possible ways to improve the model are to upgrade the unresolved gravity wave parameterization in the current version of the model. There are also plans to upgrade wam to the non-hydrostatic finite volume (FV3) dynamical core. The FV3 dynamical core is less diffusive than the current spectral version of wam, which together with increasing the model horizontal resolution, would enable a much richer wave spectrum to be supported.

The critical role of the prereversal enhancement of the zonal electric field on the behavior of ESF was recognized even before the underlying plasma instability was identified (Farley et al., 1970). The prereversal enhancement has been analyzed and interpreted theoretically by numerous investigators (Eccles, 1998; Eccles et al., 2015; Farley et al., 1986; Haerendel & Eccles, 1992; Heelis, 2004; Heelis et al., 2012; Rishbeth, 1973). The feature arises from the spatial inhomogeneity of both the conductivity and the forcing in the vicinity of the evening terminator in three dimensions and the requirements for incompressible plasma flow. The concept is straightforward, but the details have been shown to be sensitive to multiple factors. The quiet-time climatology of the prereversal enhancement is well characterized and clearly correlated with the likelihood of ESF (Chapagain et al., 2009; Fejer et al., 1979, 1999, 2008; Scherliess & Fejer, 1999; Stolle et al., 2008). Numerical simulations are increasingly able to reproduce both the typical morphology of the prereversal enhancement and, through data assimilation, its day-to-day behavior (Chen et al., 2017; Fesen et al., 2000; Richmond et al., 2015; Richmond & Fang, 2015). Progress has also been made in understanding enhancements in the vertical plasma drifts at the equator around midnight that influence postsunset ESF that have not been investigated here (Fang et al., 2016). We reiterate here that not only the strength but also the onset and duration of the prereversal enhancement must be captured for a model to be considered accurate.

Chen et al. (2017) highlight the necessity of strong thermospheric winds near the terminator for the generation of a robust prereversal enhancement. Richmond and Fang (2015) showed that the thermospheric winds at latitudes encompassing the EIA are mainly responsible for driving the prereversal enhancement and the evening vortex. Convection was also found to be regulated by the  $E$  region through ion drag associated with the Cowling current.

Additionally, thermospheric winds and the associated, imperfectly efficient  $F$ -region dynamo is responsible for driving vertical  $F$ -region currents in the vicinity of the terminator (Haerendel & Eccles, 1992; Haerendel et al., 1992). Vertical currents destabilize the ionosphere at the base of the  $F$ -region, giving rise to bottom-type irregularity layers (Woodman and La Hoz, 1976; Woodman, 2009). The fast-growing irregularities are concentrated at the top of the valley region or base of the bottomside, where they are confined, but serve to precondition the ionosphere for collisional interchange instability (Hysell et al., 2020; Hysell & Kudeki, 2004). Without them, it would not be possible for density depletions associated with ESF conditions to develop and penetrate to the topside within 90 min after sunset. Richmond et al. (2015) found that the time lag in the onset of eastward thermospheric winds after sunset is reduced by ion drag and that the effect also contributes to vertical shear in the postsunset zonal winds. Surprisingly, however, westward convection in the postsunset bottomside was found to weaken rather than strengthen the prereversal enhancement, so the two important effects must be, in a complicated way, competing.

That the zonal winds do not appear in the conventional linear growth rate expression often used as a forecast tool highlights the limitations of the tool. Accurate forecasts of ESF conditions will require, at a minimum, accurate forecasts of the zonal electric field behavior around sunset as well as the behavior of the zonal thermospheric winds. The crucial factor appears to be the timing of the reversal of the winds from westward to eastward relative to the onset time and duration of the prereversal enhancement and how they combine to produce the evening vortex. The shape of the local background plasma density profile in the valley region was not found to be especially important in the current study, although more investigation around this point is required.

### Data Availability Statement

Data used for this publication are available through the Madrigal database (see <http://www.openmadrigal.org/>).

### Acknowledgments

This project is supported by NSF award no. AGS-2028032 to Cornell University and the University of Colorado Boulder. WAM-IPE results are available via the <http://doi.org/10.5281/zenodo.6773024>. The Jicamarca Radio Observatory is a facility of the Instituto Geofísico del Perú operated with support from NSF award AGS-1732209 through Cornell. The help of the staff is much appreciated.

### References

- Ajith, K. K., Ram, S. T., Yamamoto, M., Otsuka, Y., & Niranjana, K. (2016). On the fresh development of equatorial plasma bubbles around the midnight hours of June solstice. *Journal of Geophysical Research*, *121*(9), 9051–9062. <https://doi.org/10.1002/2016JA023024>
- Akmaev, R. A., & Juang, H. M. H. (2008). Using enthalpy as a prognostic variable in atmospheric modelling with variable composition. *Quarterly Journal of the Royal Meteorological Society*, *134*(637), 2193–2197. <https://doi.org/10.1002/qj.345>
- Bilitza, D., Altadill, D., Reinisch, B., Galkin, I., Shubin, V., & Truhlik, V. (2016). The international reference ionosphere: Model update 2016. *Egu general assembly conference abstracts*, *18*, 9671.
- Chapagain, N. P., Fejer, B. G., & Chau, J. L. (2009). Climatology of postsunset equatorial spread *F* over Jicamarca. *Journal of Geophysical Research*, *A07307*(A7). <https://doi.org/10.1029/2008JA013911>
- Chen, C. H., Lin, C., Chen, W. H., & Matsuo, T. (2017). Modeling the ionospheric prereversal enhancement by using coupled thermosphere-ionosphere data assimilation. *Geophysical Research Letters*, *44*(4), 1652–1659. <https://doi.org/10.1002/2016GL071812>
- Dao, E., Seyler, C. E., & Kelley, M. C. (2013). Three-dimensional modeling of the electromagnetic characteristics of equatorial plasma depletions. *Journal of Geophysical Research*, *118*(6), 3505–3514. <https://doi.org/10.1002/jgra.50216>
- Derghazarian, S., Hysell, D. L., & Varney, R. H. (2021). Topside measurements at Jicamarca during the 2019–2020 deep solar minimum. *Journal of Geophysical Research*, *126*(12). <https://doi.org/10.1029/2021JA029695>
- Drake, J. F., & Huba, J. D. (1987). Dynamics of three-dimensional ionospheric plasma clouds. *Geophysical Research Letters*, *58*(3), 278–281. <https://doi.org/10.1103/physrevlett.58.278>
- Drob, D. P., Emmert, J. T., Meriwether, J. W., Makela, J. J., Doornbos, E., Conde, M., et al. (2015). An update to the Horizontal Wind Model (HWM): The quiet time thermosphere. *Earth and Space Science*, *2*(7), 301–319. <https://doi.org/10.1002/2014EA000089>
- Eccles, J. V. (1998). A simple model of low-latitude electric fields. *Journal of Geophysical Research*, *103*(26), 699–26708. <https://doi.org/10.1029/98ja02657>
- Eccles, J. V., Maurice, J. P. S., & Schunk, R. W. (2015). Mechanisms underlying the prereversal enhancement of the vertical plasma drift in the low-latitude ionosphere. *Journal of Geophysical Research*, *120*(6), 4950–4970. <https://doi.org/10.1002/2014JA020664>
- Emmert, J. T., Drob, D. P., Picone, J. M., Siskind, D. E., Jones, M., Jr., Mlyneczek, M. G., et al. (2021). NRLMSIS 2.0: A whole-atmosphere empirical model of temperature and neutral species densities. *Earth and Space Science*, *8*(3), e2020EA001321. <https://doi.org/10.1029/2020EA001321>
- Fang, T. W., Akmaev, R. A., Stoneback, R. A., Fuller-Rowell, T., Wang, H., & Wu, F. (2016). Impact of midnight thermosphere dynamics on the equatorial ionospheric vertical drifts. *Journal of Geophysical Research*, *121*(5), 4858–4868. <https://doi.org/10.1002/2015JA022282>
- Fang, T. W., Fuller-Rowell, T., Yudin, V., Matsuo, T., & Viereck, R. (2018). Quantifying the sources of ionosphere day-to-day variability. *Journal of Geophysical Research*, *123*(11), 9682–9696. <https://doi.org/10.1029/2018JA025525>
- Farley, D. T., Balsley, B. B., Woodman, R. F., & McClure, J. P. (1970). Equatorial spread *F*: Implications of VHF radar observations. *Journal of Geophysical Research*, *75*(34), 7199–7216. <https://doi.org/10.1029/ja075i034p07199>
- Farley, D. T., Bonelli, E., Fejer, B. G., & Larsen, M. F. (1986). The prereversal enhancement of the zonal electric field in the equatorial ionosphere. *Journal of Geophysical Research*, *91*(A12), 13723. <https://doi.org/10.1029/ja091ia12p13723>
- Fejer, B. G. (1997). The electrodynamics of the low-latitude ionosphere: Recent results and future challenges. *Journal of Atmospheric and Terrestrial Physics*, *59*(13), 1465–1482. [https://doi.org/10.1016/s1364-6826\(96\)00149-6](https://doi.org/10.1016/s1364-6826(96)00149-6)
- Fejer, B. G., Farley, D. T., Woodman, R. F., & Calderon, C. (1979). Dependence of equatorial *F*-region vertical drifts on season and solar cycle. *Journal of Geophysical Research*, *84*(A10), 5792. <https://doi.org/10.1029/ja084ia10p05792>
- Fejer, B. G., Jesen, J. W., & Su, S. Y. (2008). Quiet time equatorial *F* region vertical plasma drift model derived from ROCSAT-1 observations. *Journal of Geophysical Research*, *113*(A5). <https://doi.org/10.1029/2007JA012801>
- Fejer, B. G., Scherliess, L., & de Paula, E. R. (1999). Effects of the vertical plasma drift velocity on the generation and evolution of equatorial spread *F*. *Journal of Geophysical Research*, *104*(19), 859–19869. <https://doi.org/10.1029/1999ja000271>
- Fesen, C. G., Roble, R. G., Richmond, A. D., Crowley, G., & Fejer, B. G. (2000). Simulation of the pre-reversal enhancement in the low latitude vertical ion drifts. *Geophysical Research Letters*, *27*(13), 1851–1854. <https://doi.org/10.1029/2000gl000061>
- Flaherty, J. P., Seyler, C. E., & Trefethen, L. N. (1999). Large-amplitude transient growth in the linear evolution of equatorial spread *F* with a sheared zonal flow. *Journal of Geophysical Research*, *104*(A4), 6843–6857. <https://doi.org/10.1029/1998ja00178>
- Ge, S., Xu, T., Li, H., Zhu, M., Hu, Y., & Meng, L. (2018). Preliminary analysis of the effects of magnetic declination on flux-tube integrated linear growth rate of generalized Rayleigh-Taylor instability. In *12th International Symposium on Antennas, Propagation and EM Theory (ISAPE)*, (pp. 1–4). <https://doi.org/10.1109/ISAPE.2018.8634274>
- Guzdar, P. N., Satyanarayana, P., Huba, J. D., & Ossakow, S. L. (1983). Influence of velocity shear on Rayleigh-Taylor instability. *Geophysical Research Letters*, *9*(5), 547–550. <https://doi.org/10.1029/gl009i005p00547>
- Haerendel, G. (1973). *Theory of equatorial spread-F*. Max Planck Institute for Extraterrestrial Physics.
- Haerendel, G., & Eccles, J. V. (1992). The role of the equatorial electrojet in the evening ionosphere. *Journal of Geophysical Research*, *97*(A2), 1181. <https://doi.org/10.1029/91ja02227>
- Haerendel, G., Eccles, J. V., & Cakir, S. (1992). Theory for modeling the equatorial evening ionosphere and the origin of the shear in the horizontal plasma flow. *Journal of Geophysical Research*, *97*(A2), 1209. <https://doi.org/10.1029/91ja02226>
- Heelis, R. A. (2004). Electrodynamics in the low and middle latitude ionosphere: A tutorial. *Journal of Atmospheric and Solar-Terrestrial Physics*, *66*(10), 825–838. <https://doi.org/10.1016/j.jastp.2004.01.034>
- Heelis, R. A., Crowley, G., Rodrigues, F., Reynolds, A., Wilder, R., Azeem, I., & Maute, A. (2012). The role of zonal winds in the production of a pre-reversal enhancement in the vertical ion drift in the low latitude ionosphere. *Journal of Geophysical Research*, *117*(A08308). <https://doi.org/10.1029/2012JA017547>
- Huba, J. D., Bernhardt, P. A., Ossakow, S. L., & Zalesak, S. T. (1996). The Rayleigh Taylor instability is not damped by recombination in the *F* region. *Journal of Geophysical Research*, *101*(A11), 24553–24556. <https://doi.org/10.1029/96ja02527>
- Hysell, D. L., & Burcham, J. (2002). Long term studies of equatorial spread *F* using the JULIA radar at Jicamarca. *Journal of Atmospheric and Solar-Terrestrial Physics*, *64*(12), 1531–1543. [https://doi.org/10.1016/S1364-6826\(02\)00091-3](https://doi.org/10.1016/S1364-6826(02)00091-3)
- Hysell, D. L., & Kudeki, E. (2004). Collisional shear instability in the equatorial *F* region ionosphere. *Journal of Geophysical Research*, *109*, A11301. <https://doi.org/10.1029/2004JA010636>
- Hysell, D. L., Larsen, M. F., Fritts, D. C., Laughman, B., & Sulzer, M. P. (2018). Major upwelling and overturning in the mid-latitude *F* region ionosphere. *Nature Communications*, *9*(3326). <https://doi.org/10.1038/s41467-018-05809-x>
- Hysell, D. L., Larsen, M. F., Swenson, C. M., Wheeler, T. F., & Pfaff, R. F. (2006). Shear flow effects at the onset of equatorial spread *F*. *Journal of Geophysical Research*, *111*(A12), A11317. <https://doi.org/10.1029/2006JA011923>

- Hysell, D. L., Milla, M. A., Condori, L., & Vierinen, J. (2015). Data-driven numerical simulations of equatorial spread  $F$  in the Peruvian sector 3: Solstice. *Journal of Geophysical Research*, *120*(12), 10809–10822. <https://doi.org/10.1002/2015JA021877>
- Hysell, D. L., Rao, S., Groves, K. M., & Larsen, M. F. (2020). Radar investigation of postsunset equatorial ionospheric stability over Kwajalein during project WINDY. *Journal of Geophysical Research*, *125*(6). <https://doi.org/10.1029/2020ja027997>
- Hysell, D. L., & Seyler, C. E. (1998). A renormalization group approach to estimation of anomalous diffusion in the unstable equatorial  $F$  region. *Journal of Geophysical Research*, *103*(26), 731–26737. <https://doi.org/10.1029/98ja02616>
- Kelley, M. C., Makela, J. J., de la Beaujardiere, O., & Retterer, J. (2011). Convective ionospheric storms: A review. *Reviews of Geophysics*, *49*, RG2003. <https://doi.org/10.1029/2010RG000340>
- Keskinen, M. J., Ossakow, S. L., & Fejer, B. G. (2003). Three-dimensional nonlinear evolution of equatorial ionospheric spread- $F$  bubbles. *Geophysical Research Letters*, *30*(16), 1855. <https://doi.org/10.1029/2003GL017418>
- Kil, H. (2015). The morphology of equatorial plasma bubbles - A review. *J. Astro Space Sci.*, *32*(1), 13–19. <https://doi.org/10.5140/JASS.2015.32.1.13>
- Ossakow, S. L. (1981). Spread  $F$  theories – A review. *Journal of Atmospheric and Terrestrial Physics*, *43*(5–6), 437–452. [https://doi.org/10.1016/0021-9169\(81\)90107-0](https://doi.org/10.1016/0021-9169(81)90107-0)
- Richards, P. G., Meier, R. R., & Wilkinson, P. J. (2010). On the consistency of satellite measurements of thermospheric composition and solar EUV irradiance with Australian ionosonde electron density data. *Journal of Geophysical Research*, *115*, A10309. <https://doi.org/10.1029/2010JA015368>
- Richmond, A. D. (1995). Ionospheric electrodynamics using magnetic apex coordinates. *Journal of Geomagnetism and Geoelectricity*, *47*(2), 191–212. <https://doi.org/10.5636/jgg.47.191>
- Richmond, A. D., & Fang, T. W. (2015). Electrodynamics of the equatorial evening ionosphere: 2. Conductivity influences on convection, current, and electrodynamic energy flow. *Journal of Geophysical Research*, *120*(3), 2133–2147. <https://doi.org/10.1002/2014JA020935>
- Richmond, A. D., Fang, T. W., & Maute, A. (2015). Electrodynamics of the equatorial evening ionosphere: 1. Importance of winds in different regions. *Journal of Geophysical Research*, *120*(3), 2118–2132. <https://doi.org/10.1002/2014JA020934>
- Rishbeth, H. (1973). Further studies of directional  $F$ -layer currents. *Planetary and Space Science*, *19*, 357–369.
- Satyanarayana, P., Guzdar, P. N., Huba, J. D., & Ossakow, S. L. (1984). Rayleigh-Taylor instability in the presence of a stratified shear layer. *Journal of Geophysical Research*, *89*(A5), 2945. <https://doi.org/10.1029/ja089ia05p02945>
- Scherliess, L., & Fejer, B. G. (1999). Radar and satellite global equatorial  $F$  region vertical drift model. *Journal of Geophysical Research*, *105*(A4), 6829–6842. <https://doi.org/10.1029/1999ja900025>
- Shinagawa, H., Jidekatsu, J., Yasunobu, M. T., Yokoyama, H. F., & Otsuka, Y. (2018). Daily and seasonal variations in the linear growth rate of the Rayleigh-Taylor instability in the ionosphere obtained with GAIA. *Progress in Earth and Planetary Science*, *5*(16). <https://doi.org/10.1186/s40645-018-0175-8>
- Smith, J. M., Rodrigues, F. S., Fejer, B. G., & Milla, M. A. (2016). Coherent and incoherent scatter radar study of the climatology and day-to-day variability of mean  $F$  region vertical drifts and equatorial spread  $F$ . *Journal of Geophysical Research*, *121*(2), 1466–1482. <https://doi.org/10.1002/2015JA021934>
- Stolle, C., Lühr, H., & Fejer, B. G. (2008). Relation between the occurrence rate of ESF and the equatorial vertical plasma drift velocity at sunset derived from global observations. *Annales Geophysicae*, *26*(12), 3979–3988. <https://doi.org/10.5194/angeo-26-3979-2008>
- Sultan, P. J. (1996). Linear theory and modeling of the Rayleigh-Taylor instability leading to the occurrence of equatorial spread  $F$ . *Journal of Geophysical Research*, *101*(26), 875–26891. <https://doi.org/10.1029/96ja00682>
- Tang, L., Chen, W., Louis, O. P., & Chen, M. (2020). Study on seasonal variations of plasma bubble occurrence over Hong Kong area using GNSS observations. *Remote Sensing*, *12*(15), 2423. <https://doi.org/10.3390/rs12152423>
- Trac, H., & Pen, U. L. (2003). A primer on Eulerian computational fluid dynamics for astrophysicists. *Astrophysics*, *115*(805), 303–321. <https://doi.org/10.1086/367747>
- Trefethen, L. N., Trefethen, A. E., Reddy, S. C., & Driscoll, T. A. (1993). Hydrodynamic stability without eigenvalues. *Science*, *261*(5121), 578–584. <https://doi.org/10.1126/science.261.5121.578>
- Varney, R. H., Hysell, D., & Huba, J. (2013). Sources of variability in equatorial topside ionospheric and plasmaspheric temperatures. *Journal of Atmospheric and Solar-Terrestrial Physics*, *103*, 83–93. <https://doi.org/10.1016/j.jastp.2012.12.024>
- Varney, R. H., Swartz, W., Hysell, D., & Huba, J. (2012). SAMI2-PE: A model of the ionosphere including multi-stream interhemispheric photoelectron transport. *Journal of Geophysical Research*, *117*(A06322). <https://doi.org/10.1029/2011JA017280>
- Weimer, D. R. (2005). Improved ionospheric electrodynamic models and application to calculating Joule heating rates. *Journal of Geophysical Research*, *110*, A05306. <https://doi.org/10.1029/2004JA010884>
- Woodman, R. F. (2009). Spread  $F$ - An old equatorial aeronomy problem finally resolved? *Annales Geophysicae*, *27*(5), 1915–1934. <https://doi.org/10.5194/angeo-27-1915-2009>
- Woodman, R. F., & La Hoz, C. (1976). Radar observations of  $F$  region equatorial irregularities. *Journal of Geophysical Research*, *81*(31), 5447–5466. <https://doi.org/10.1029/ja081i031p05447>
- Wu, Q. (2015). Longitudinal and seasonal variation of the equatorial flux tube integrated Rayleigh-Taylor instability growth rate. *Journal of Geophysical Research*, *120*(9), 7952–7957. <https://doi.org/10.1002/2015JA021553>
- Zalesak, S. T., Ossakow, S. L., & Chaturvedi, P. K. (1982). Nonlinear equatorial spread  $F$  - The effect of neutral winds and background Pedersen conductivity. *Journal of Geophysical Research*, *87*(A1), 151–166. <https://doi.org/10.1029/ja087ia01p00151>
- Zargham, S., & Seyler, C. E. (1987). Collisional interchange instability, I. Numerical simulations of intermediate-scale irregularities. *Journal of Geophysical Research*, *92*(A9), 10073. <https://doi.org/10.1029/ja092ia09p10073>
- Zargham, S., & Seyler, C. E. (1989). Collisional and inertial dynamics of the ionospheric interchange instability. *Journal of Geophysical Research*, *94*(A7), 9009. <https://doi.org/10.1029/ja094ia07p09009>